THE INFRARED SPECTRUM OF PROTONATED OVALENE IN SOLID PARA-HYDROGEN AND ITS POSSIBLE CONTRIBUTION TO INTERSTELLAR UNIDENTIFIED INFRARED EMISSION

Masashi Tsuge[1], Mohammed Bahou[1], Yu-Jong Wu[2], Louis Allamandola[3], and Yuan-Pern Lee[1,4]

[1] Department of Applied Chemistry and Institute of Molecular Sciences, National Chiao Tung University, 1001, Ta-Hsueh Road, Hsinchu 30010, Taiwan; tsuge@nctu.edu.tw, yplee@mail.nctu.edu.tw
[2] National Synchrotron Radiation Research Center, 101, Hsin-Ann Road, Hsinchu 30076, Taiwan
[3] The Astrophysics and Astrochemistry Laboratory, NASA Ames Research Center, Moffett Field, CA 94035, USA
[4] Institute of Molecular Sciences, Academia Sinica, Taipei 10617, Taiwan

ABSTRACT

The mid-infrared emission from galactic objects, including reflection nebulae, planetary nebulae, proto-planetary nebulae, molecular clouds, etc, as well as external galaxies, is dominated by the unidentified infrared (UIR) emission bands. Large protonated polycyclic aromatic hydrocarbons (H^+PAHs) were proposed as possible carriers, but no spectrum of an H^+PAH has been shown to exactly match the UIR bands. Here, we report the IR spectrum of protonated ovalene (7-$C_{32}H_{15}^+$) measured in a *para*-hydrogen (*p*-H_2) matrix at 3.2 K, generated by bombarding a mixture of ovalene and *p*-H_2 with electrons during matrix deposition. Spectral assignments were made based on the expected chemistry and on the spectra simulated with the wavenumbers and infrared intensities predicted with the B3PW91/6-311++G(2d,2p) method. The close resemblance of the observed spectral pattern to that of the UIR bands suggests that protonated ovalene may contribute to the UIR emission, particularly from objects that emit Class A spectra, such as the IRIS reflection nebula, NGC 7023.

Key words: astrochemistry – infrared: ISM – ISM: lines and bands – ISM: molecules

Supporting material: machine-readable tables

1. INTRODUCTION

The near-infrared (near-IR) and mid-infrared (mid-IR) emission from many astronomical objects is dominated by the unidentified infrared (UIR) emission bands, which show major features at 3.3, 6.2, 7.7, 8.6, and 11.2 μm (Willner 1984; Tielens 2011). For instance, a variety of galactic objects, including reflection nebulae (e.g., NGC 7023 and NGC 2023), planetary nebulae (e.g., NGC 7027 and BD 30″3639), and external galaxies, emit UIR. Because these features are characteristic of the CH stretching, CC stretching, and CH bending modes of aromatic compounds, polycyclic aromatic hydrocarbons (PAHs) and their derivatives have been proposed to be responsible for these UIR bands upon UV excitation (Leger & Puget 1984; Allamandola et al. 1985, 1989; Puget & Léger 1989). However, no PAH has been positively identified to be responsible for the UIR bands (Cook et al. 1996). The ions of PAHs, including the PAH cation (designated PAH^+) and protonated PAH (designated H^+PAH), are among the PAH derivatives proposed to be potential carriers of the UIR emission (Hudgins et al. 2001; Pathak & Sarre 2008; Dopfer 2011). The H^+PAHs are closed-shell stable molecules that might be produced in interstellar space from proton-transfer reactions of PAHs with abundant proton sources such as H_3^+ and from capture of a hydrogen atom by a PAH^+. Furthermore, theoretical studies indicate that the electronic excitation spectra of H^+PAHs in the visible region might be responsible for some of the diffuse interstellar bands (DIB) (Snow et al. 1998; Hammonds et al. 2009). Ricca et al. suggested that, based on density functional theory (DFT) calculations, H^+PAHs with more than 50 carbon atoms cannot be major contributors to the 6.2 μm band (Class A) (Ricca et al. 2011); however, these species are currently too large for experimental testing and comparison. PAHs have also been proposed to play critical roles in the production of the H_2 molecule in the interstellar

medium, a very important astrochemical process (Bauschlicher 1998; Skov et al. 2014; Boschman et al. 2015). One proposed model for formation of H_2 includes a reaction initiated by capture of an H atom by a PAH or PAH^+ to form a mono-hydrogenated PAH (designated HPAH) or H^+PAH, followed by elimination of H_2 when a second H atom binds to this HPAH or H^+PAH.

Measuring the mid-IR spectra of large H^+PAHs in a laboratory is challenging. There are two major techniques to obtain mid-IR spectra of H^+PAHs. In the first technique, the infrared multi-photon dissociation method (Jones et al. 2003; Knorke et al. 2009) typically yields broad spectral bands that are redshifted from mid-IR absorption bands. The second method employs infrared photodissociation of tagged H^+PAHs (Solcà & Dopfer 2002; Douberly et al. 2008; Ricks et al. 2009; Dopfer 2011). Because spectra obtained by this method are action spectra, which record the variation of signals upon infrared irradiation and depend on both the absorption coefficient and dissociation yield, the relative intensities observed in these action spectra might not reflect the intrinsic absorption intensities. Furthermore, it is difficult to tag a large H^+PAH with a species such as Ar because vibrational cooling is not efficient in a supersonic jet and the internal energy of the parent H^+PAH might exceed the binding energy between Ar and the H^+PAH; the largest Ar-tagged H^+PAH studied with this method is protonated naphthalene ($C_{10}H_9^+$) (Ricks et al. 2009).

Recently, we have developed a new method to investigate the mid-IR spectra of H^+PAHs and HPAHs using electron bombardment during deposition of PAH diluted in *para*-hydrogen (*p*-H_2) at 3.2 K (Bahou et al. 2014a). The bombardment of *p*-H_2 with electrons produces H_3^+ and H, which subsequently react with PAH to form H^+PAH and HPAH which are trapped in the *p*-H_2 matrix. This method has been
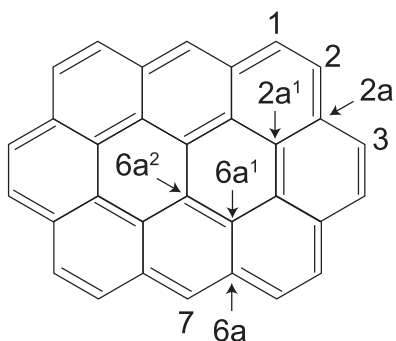
Figure 1. Possible protonation sites of ovalene ($C_{32}H_{14}$). The position numbers conform to IUPAC recommendations.

successfully applied to benzene (C_6H_6) (Bahou et al. 2012), naphthalene ($C_{10}H_8$) (Bahou et al. 2013a), pyrene ($C_{16}H_{10}$) (Bahou et al. 2013b), and coronene ($C_{24}H_{12}$) (Bahou et al. 2014b) to obtain mid-IR spectra of the protonated species and their neutral counterparts with narrow lines and excellent signal-to-noise ratios. Furthermore, this method does not induce significant fragmentation nor further hydrogenation of PAHs and H^+PAHs.

To date, laboratory mid-IR spectra of H^+PAHs were reported for protonated naphthalene (Ricks et al. 2009; Bahou et al. 2013a), pyrene (Dopfer 2011; Bahou et al. 2013b), and coronene (Dopfer 2011; Bahou et al. 2014b). As the size of the aromatic molecules increases, the infrared absorption bands of these species shift toward, but do not yet match, the positions of the UIR bands. These observations led to the suggestion that H^+PAHs have the chromophore required to account for prominent features of the UIR bands and that the mid-IR spectrum of larger H^+PAHs might show better agreement with the UIR bands (Bahou et al. 2014b). Unfortunately, these H^+PAHs whose spectra have been measured are smaller than those expected to survive irradiation in the interstellar medium (Allamandola et al. 1989; Puget & Léger 1989). Laboratory observations of mid-IR spectra of larger H^+PAHs are highly desirable.

Ovalene ($C_{32}H_{14}$), of symmetry point group D_{2h}, is a peri-condensed PAH with ten benzenoid rings (Figure 1). The mid-IR and far-IR spectra of gaseous, solid, and matrix-isolated ovalene were reported (Joblin et al. 1994; Mattioda et al. 2009) and compared with harmonic vibrational wavenumbers calculated with several DFT methods (Langhoff 1996; Bauschlicher & Bakes 2000; Mattioda et al. 2009). The electronic spectra of larger PAH ions, including the ovalene cation and anion, have been investigated theoretically (Weisman et al. 2003; Malloci et al. 2004, 2005; Steglich et al. 2011). The UV/vis/near-IR spectra of matrix-isolated ovalene and its cation have been reported (Ehrenfreund et al. 1992; Ruiterkamp et al. 2002), but the spectral features of these species agree poorly with the DIBs. To our knowledge, the experimental mid-IR spectrum of protonated ovalene has not been reported.

In this work, we extended our investigations to protonated ovalene, $C_{32}H_{15}^+$, a species that is at the lower end in terms of the size of PAH-related species that are likely to survive the interstellar radiation field. The mid-IR spectrum of $7\text{-}C_{32}H_{15}^+$ (see Figure 1 for protonation site) is recorded and assigned with the aid of theoretical calculations. The laboratory mid-IR spectrum of $7\text{-}C_{32}H_{15}^+$ is compared with UIR observations to

demonstrate that $C_{32}H_{15}^+$ is the first H^+PAH that convincingly matches the UIR bands.

2. METHODS

The matrix-isolation system for mid-IR absorption and the p-H_2 converter used in this work have been described elsewhere (Lee et al. 2006; Bahou et al. 2012, 2014a). A gold-plated flat copper substrate, cooled to 3.2 K with a closed-cycle helium refrigerator system (SHI, RDK-415D), served as both the matrix sample substrate and the mirror to reflect the incident mid-IR beam to the detector. Absorption spectra spanning 450–5000 cm^{-1} were recorded with a Fourier-transform infrared spectrometer (Bomem, DA8) equipped with a KBr beamsplitter and a HgCdTe detector cooled to 77 K. Typically, 600 scans at resolution 0.25 cm^{-1} were recorded at each stage of the experiment.

The gaseous mixture of ovalene/p-H_2 was deposited onto the substrate at 3.2 K over a period of 7 hr at flow rate of $\sim$13 mmol hr^{-1}. Ovalene was heated to 473 K in a copper tube (internal diameter 10 mm) to increase its vapor pressure. Because of the small vapor pressure, we were unable to determine accurately the mixing ratio of ovalene/p-H_2. Employing the theoretically predicted IR intensities of some intense bands of ovalene, we estimated the concentration of ovalene in p-H_2 to be 30 $\pm$ 15 ppm. In experiments to produce protonated ovalene, the matrix was bombarded with an electron beam during deposition; an electron gun (Kimball Physics, Model EFG-7) provided a 60 μA electron beam with kinetic energy of 250 eV.

p-H_2 was prepared in a p-H_2 converter equipped with a copper cell filled with iron (III) oxide catalyst (Aldrich) and cooled with a closed-cycle helium refrigerator. Normal hydrogen (99.9999%) was passed through a trap at 77 K before entering the p-H_2 converter. The efficiency of conversion depends on the temperature of the catalyst; at a temperature of 11–13 K, our operating condition, the concentration of *ortho*-H_2 was less than 100 ppm.

Quantum-chemical calculations were performed with Gaussian 09 (Revisions C.01 and D.01) (Frisch et al. 2009). Geometrical optimization and harmonic vibrational analysis were performed with the B3PW91 (Becke's three-parameter hybrid exchange functional and Perdew/Wang correlation functional) method (Becke 1993; Perdew et al. 1996). The standard split valence 6-31G(d,p) and 6-311++G(2d,2p) basis sets were used. The harmonic vibrational wavenumbers were scaled with factors of 0.958 and 0.978 for the values >2500 cm^{-1} and <2500 cm^{-1}, respectively; these factors are the same as those used for coronene (Bahou et al. 2014b). In addition, anharmonic vibrational analyses, which provided the wavenumbers and intensities of the fundamental, overtone, and combination bands, were performed with a 6-31G(d,p) basis set (Bloino & Barone 2012).

3. RESULTS AND DISCUSSION

3.1. Computational Results

Ovalene has nine distinct carbon sites for protonation (Figure 1). The most stable isomer of $C_{32}H_{15}^+$ is $7\text{-}C_{32}H_{15}^+$, which is 46–142 kJ mol^{-1} more stable than the other isomers (Table 1). Our results agree with those calculated for 2- and $7\text{-}C_{32}H_{15}^+$ by Bauschlicher and Bakes with the B3LYP/4-31G method (Bauschlicher & Bakes 2000). The energetics to form

Table 1
Relative Energies, Formation Energies, and Isomerization Barriers
(in kJ mol^{-1}) of Protonated Ovalene Calculated with the
B3PW91/6-311++G(2d,2p) Method

Isomer[a]	$C_{32}H_{15}^+$	
	Relative Energy	Bauschlicher & Bakes (2000)[b]
7-	0 (525)[c]	0
1-	46 (479)	<79
2-	71 (454)	79
3-	48 (477)	<79
2a-	108 (418)	…
6a-	138 (387)	…
2a^1-	142 (384)	…
6a^1-	122 (403)	…
6a^2-	136 (389)	…
TS (1–2)	126	…
TS (2–2a)	162	…
TS (2a–3)	147	…
TS (3–4)	126	…
TS (6–6a)	168	…
TS (6a–7)	147	…

Notes.
[a] See Figure 1 for positions.
[b] Calculated with the B3LYP/4-31G method.
[c] Exothermicity of the reaction $C_{32}H_{14} + H_3^+ \rightarrow C_{32}H_{15}^+ + H_2$ is given in parentheses.

various protonated ovalene isomers, including the transition states (TS) in reactions at the outer edges, were calculated with the B3PW91/6-311++G(2d,2p) method; the results are also listed in Table 1.

The proton-transfer reactions $C_{32}H_{14} + H_3^+ \rightarrow C_{32}H_{15}^+ + H_2$ have no barrier; the exothermicity of these reactions ranges from 384 kJ mol^{-1} for formation of $2a^1$-$C_{32}H_{15}^+$ to 525 kJ mol^{-1} for 7-$C_{32}H_{15}^+$. The heights of the barriers for the interconversion of isomers of protonated ovalene are smaller than the exothermicity of the proton-transfer reactions, as shown in Figure 2. A proton attached to ovalene might hence be liable to find a more stable site before being quenched in solid p-H_2; therefore, the formation of 7-$C_{32}H_{15}^+$ is expected to be the most favorable path.

The stick spectra of $C_{32}H_{15}^+$ isomers, presenting scaled harmonic vibrational wavenumbers predicted with the B3PW91/6-311++G(2d,2p) method, are shown in Figure 3. We applied scaling factors of 0.958 and 0.978 for harmonic vibrational wavenumbers in regions above and below 2500 cm^{-1}, respectively; these values are the same as those used for coronene ($C_{24}H_{12}$) (Bahou et al. 2014b). Lists of the vibrational wavenumbers and IR intensities of 7-$C_{32}H_{15}^+$ and 1-, 2-, and 3-$C_{32}H_{15}^+$ are available in Tables 2 and 3. For all isomers, moderately intense lines (IR intensity 50–100 km mol^{-1}) associated with the out-of-plane CH bending modes are predicted to occur between 800 and 900 cm^{-1}. An additional moderately intense line associated with an out-of-plane CH bending mode is predicted near 1010 cm^{-1} for 1-, 2-, and 3-$C_{32}H_{15}^+$. Lines predicted in the 1500–1600, 1300–1400, 1150–1250 cm^{-1} regions are associated with the CC stretching, ring deformation, and in-plane CH bending modes, respectively. The aromatic CH stretching modes are predicted in the region 3050–3080 cm^{-1}. The characteristic CH$_2$ scissoring mode, which is unique for the protonation at a site on the unfused edges, is predicted at 1340–1374 cm^{-1} for the 1-, 2-, 3-, and 7-$C_{32}H_{15}^+$ isomers with IR intensities greater
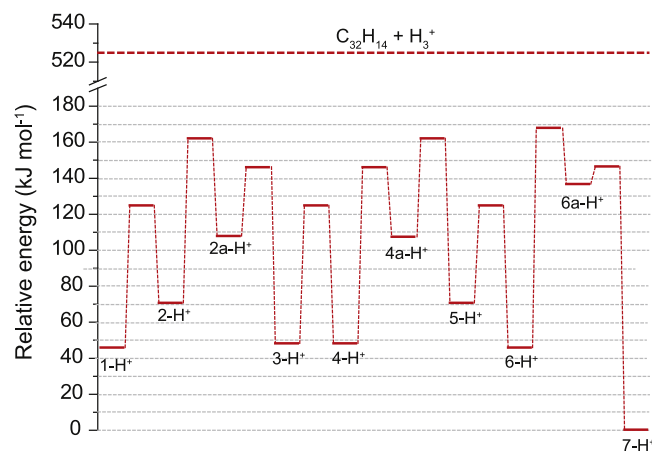

Figure 2. Potential-energy diagram for protonated ovalene isomers x-$C_{32}H_{15}^+$ (x = 1, 2, 2a, 3, 4, 4a, 5, 6, 6a, and 7) and transition states connecting these isomers calculated with the B3PW91/6-311++G(2d,2p) method. The energy level indicated as x-H^+ corresponds to the energy of a "x-$C_{32}H_{15}^+$ + H_2" pair relative to the most stable "7-$C_{32}H_{15}^+$ + H_2" pair. Calculated values are also listed in Table 1. Note that 1- and 6-, 2- and 5-, 2a- and 4a-, and 3- and 4- are pairs of equivalent isomers.

than 90 km mol^{-1}. Other characteristic CH$_2$ stretching modes are in the 2850–2900 cm^{-1} region, but their intensities are small (2–15 km mol^{-1}). The CH stretching mode associated with the proton attached on the fused edges and inner hexagons (i.e., positions 2a-, 6a-, 2a^1-, 6a^1-, and 6a^2-) is predicted to fall between 2650 and 2710 cm^{-1} with an intensity of ~30 km mol^{-1}, significantly distinct from the weaker lines in the 2850–2900 cm^{-1} region for 1-, 2-, 3-, and 7-$C_{32}H_{15}^+$.

3.2. Experimental Results

A partial IR spectrum after deposition is shown in Figure 4(a); spectra in the region 2750–3100 cm^{-1} are shown in Figure 5. In addition to intense lines of parent ovalene (marked P), many new lines were observed. Figure 4(b) shows the difference spectrum obtained by subtracting the spectrum recorded after deposition from the spectrum recorded after maintaining the matrix in darkness for 20 hr; lines pointing upward indicate species production whereas those pointing downward indicate destruction. The new features are classified into three groups according to the observed intensity correlations in each experimental step. Those marked with A gained intensity after the matrix was maintained in darkness, whereas those marked with A^+ (26 lines) and B^+ (7 lines) lost intensity. We distinguished between the species responsible for groups A^+ and B^+ according to their rates of decay in darkness; lines in group A^+ decay slower than those in group B^+.

After deposition, the electrons trapped in the p-H_2 matrix slowly diffuse and recombine with $C_{32}H_{15}^+$ to form $C_{32}H_{15}\cdot$. Moreover, the remaining hydrogen atoms might also diffuse to react with $C_{32}H_{14}$ to generate $C_{32}H_{15}\cdot$, as occurs with pyrene ($C_{16}H_{10}$) in a vacuum UV-irradiated H_2O matrix which slowly forms $C_{16}H_{11}$ after irradiation is stopped (Bouwman et al. 2010). The hydrogenated species $C_{32}H_{15}\cdot$ is consequently expected to increase with time, whereas the protonated species $C_{32}H_{15}^+$ to decrease with time; these types of behavior were clearly observed in our previous experiments with smaller PAHs (Bahou et al. 2013a, 2013b, 2014b). The features in group A are assigned to $C_{32}H_{15}\cdot$ and those in group A^+ are assigned to $C_{32}H_{15}^+$.
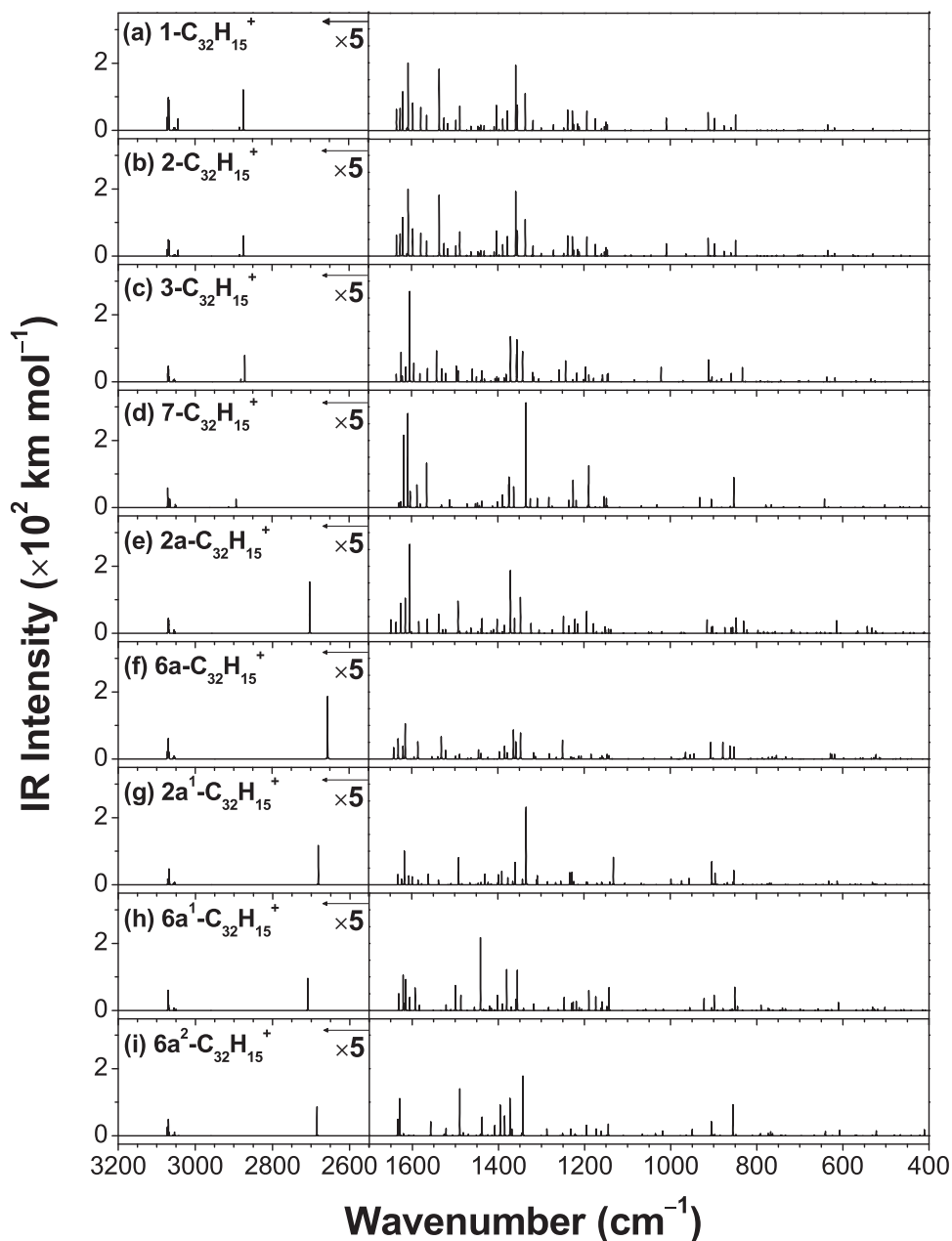
Figure 3. Scaled harmonic vibrational spectra of protonated ovalene isomers ($C_{32}H_{15}^{+}$) predicted with the B3PW91/6-311++G(2d,2p) method. Vibrational wavenumbers are scaled with factors of 0.958 and 0.978 for regions above and below 2500 cm^{-1}.

3.3. Assignments of Lines in Group A^{+} to 7-$C_{32}H_{15}^{+}$

The experimental spectrum consisting of lines in group A^{+} is compared with spectra predicted for four possible low-energy isomers of $C_{32}H_{15}^{+}$ in Figure 6. In the 800–1050 cm^{-1} region, the pattern of spectral lines for each isomer is distinct (traces (b)–(e)); the observed spectrum agrees best with that predicted for the most stable isomer 7-$C_{32}H_{15}^{+}$. Observed lines at 852.0, 907.7, and 929.0 cm^{-1} are near scaled vibrational wavenumbers at 853 (ν_{73}), 905 (ν_{72}), and 931 (ν_{71}) cm^{-1}, respectively, predicted for the out-of-plane CH bending modes of 7-$C_{32}H_{15}^{+}$ (Table 2). The 1300–1400 cm^{-1} region is also unique for 7-$C_{32}H_{15}^{+}$. An intense line at 1335.5 cm^{-1} corresponds well with the most intense line predicted at 1335 cm^{-1} for the ring deformation modes of 7-$C_{32}H_{15}^{+}$; other lines are much weaker. These lines in group A^{+} were assigned according to predicted vibrational wavenumbers and IR intensities. In addition, we tentatively assign lines at

1649.7 and 1643.3 cm^{-1} to transitions $\nu_{56} + \nu_{69}$ and $\nu_{73} + \nu_{75}$, predicted at 1675 and 1669 cm^{-1}, respectively. In the region 2800–3100 cm^{-1}, despite severe interference from absorption of ovalene, we tentatively assigned two lines at 2892.5 and 3064.7 cm^{-1} to be associated with ν_{8} and ν_{92}, predicted at 2894 and 3071 cm^{-1}, respectively. Vibrational wavenumbers and relative IR intensities of observed lines are compared with the theoretical predictions for 7-$C_{32}H_{15}^{+}$ in Table 2. The absolute percentage deviations between observed and scaled predicted vibrational wavenumbers are within 2.9%; with an average deviation of 0.8%. Nearly all features with a predicted IR intensity greater than 20 km mol^{-1} were observed. Based on the expected chemical behavior and agreement of vibrational wavenumbers and IR intensities between experiment and calculation, we assigned observed lines in group A^{+} to absorption of 7-$C_{32}H_{15}^{+}$, the most stable isomer of $C_{32}H_{15}^{+}$.

Table 2
Comparison of Experimental Observation with Vibrational Wavenumbers (cm^{-1}) and IR Intensities of 7-C$_{32}$H$_{15}^+$ Predicted with the
B3PW91/6-311++G(2d,2p) Method

Mode	Sym.	p-H$_2$	Calculation[a]	Approximate Description[b]
ν_{92}	B_2	3064.7 (w)[c,d]	3071 (3)[e]	CH stretch
ν_8	A_1	2892.5 (1)[d]	2894 (2)	CH$_2$ asym stretch
$\nu_{56} + \nu_{69}$	B_2	1649.7 (s, broad)	1675 (153)[f]	Combination
$\nu_{73} + \nu_{75}$	A_1	1643.3 (s, broad)	1669 (42)[f]	Combination
ν_{10}	A_1	1613 (s, broad)	1618 (74)	CC stretch
ν_{99}	B_2	1611 (s, broad)	1608 (91)	CC stretch
ν_{100}	B_2	1590.5 (m)	1587 (23)	CC stretch
ν_{101}	B_2	1558.2 (m)	1565 (44)	CC stretch
ν_{103}	B_2	1496.7 (m)	1512 (8)	CC stretch
ν_{109}	B_2	1405.6 (17)	1389 (12)	ring deform
ν_{110}	B_2	1355.5 (13)	1374 (29)	CH$_2$ scissor
ν_{21}	A_1	1351 (11)	1374 (21)	ring deform + ip CH bend
ν_{22}	A_1	1341.4 (12)	1363 (20)	ring deform + ip CH bend
ν_{112}	B_2	1335.5 (100)	1335 (100)	ring deform + ip CH bend +CH$_2$ wag
ν_{23}	A_1	1319.1 (26)	1324 (9)	ip CH bend
ν_{113}	B_2	1258.1 (m)[d]	1308 (10)	ring deform + ip CH bend + CH$_2$ wag
ν_{24}	A_1	1245.3 (9)[d]	1281 (11)	ring deform + ip CH bend
ν_{26}	A_1	1221.9 (16)	1225 (27)	ip CH bend
ν_{117}	B_2	1198.3 (11)	1189 (40)	ip CH bend
ν_{30}	A_1	1148.3 (8)[d]	1153 (11)	ip CH bend
ν_{120}	B_2	1143.1 (10)[d]	1148 (10)	ip CH bend
ν_{122}	B_2	1070.6 (11)	1067 (2)	ip CH bend + ring deform
ν_{33}	A_1	1026.0 (11)[d]	1030 (3)	ip CH bend + ring deform
ν_{71}	B_1	929.0 (25)	931 (11)	oop CH bend (solo)[g]
ν_{72}	B_1	907.7 (32)	905 (9)	oop CH bend (duo)[h] + CH$_2$ rock
ν_{73}	B_1	852.0 (26)	853 (29)	oop CH bend (solo + duo)[i] + CH$_2$ rock

Notes.
[a] Scaling factors 0.958 and 0.978 were used for regions above and below 2500 cm^{-1}, respectively.
[b] ip: in-plane; oop: out-of-plane.
[c] Relative intensities are listed in parentheses. For lines that could not be integrated accurately due to severe interference, approximate intensities, s (strong), m (medium), or w (weak) are given.
[d] Tentative assignments.
[e] The predicted IR intensities are normalized to 312.8 km mol^{-1}.
[f] Anharmonic wavenumbers calculated at the B3PW91/6-31G(d,p) level of theory.
[g] Involving H atoms at the 14-position.
[h] Involving H atoms at the 5-, 6-, 8-, and 9-positions.
[i] Involving H atoms at all positions excluding the 5- and 9-positions.

(This table is available in its entirety in machine-readable form.)

Lines at 1562.9, 1380.1, 1225.6, 1192.2, 1030.5, 900.9, and 892.8 cm^{-1}, assigned to group B$^+$, likely originate from cationic species other than 7-C$_{32}$H$_{15}^+$ because their intensities decay at a greater rate. Even though the most characteristic feature in group B$^+$ is observed at 1030.5 cm^{-1}, which is near lines predicted at 1021, 1009, and 1008 cm^{-1} for 2-, 1-, and 3-C$_{32}$H$_{15}^+$, respectively (Table 3), we observed no other line that is predicted to have greater intensity in the 800–900 and 1300–1650 cm^{-1} regions. These lines in group B$^+$ are hence unlikely to be due to 1-, 2-, or 3-C$_{32}$H$_{15}^+$. They might be due to fragmented cations or neutrals, but, with a limited number of observed lines, we are unable to provide definitive assignments.

3.4. Application to the UIR Bands

Observations have shown that the UIR bands can be broken down into several classes with the Class A bands always to the blue of the canonical UIR peak position (Peeters et al. 2002). The 6.2 and 11.0 μm Class A bands have proven difficult to assign to pure PAHs, suggesting that they are carried by PAH derivatives (Peeters et al. 2002; Boersma et al. 2013). Stick spectra of

protonated pyrene (1-C$_{16}$H$_{11}^+$) (Bahou et al. 2013b), coronene (1-C$_{24}$H$_{13}^+$) (Bahou et al. 2014b), and ovalene (7-C$_{32}$H$_{15}^+$) measured in p-H$_2$ matrices are compared with examples of the interstellar Class A (Cesarsky et al. 1996) and Class B (Peeters et al. 2002) UIR spectra in Figure 7. Lists of the observed lines are compared in Table 4. Keep in mind that the matrix shifts have little effect on the comparison with the broad UIR features because the wavenumber shifts induced by the p-H$_2$ matrix, similar to those induced by Ar, are smaller than 1% of the gas-phase values. We note, however, that we recorded spectra in absorption in our experiments, which should differ slightly from the emission spectra induced by UV irradiation, as in the case of the UIR bands. Several models have been presented to simulate the emission spectrum from laboratory absorption spectra or calculated spectra (Joblin et al. 1995; Cook & Saykally 1998; Pech et al. 2002; Basire et al. 2011). In general, the maxima of emission bands are slightly redshifted (10–30 cm^{-1}) from those of absorption bands because of the anharmonicity associated with the vibrationally excited states produced upon UV irradiation (Brenner & Barker 1992; Williams & Leone 1995).

Table 3
Vibrational Wavenumbers (cm^{-1}) and Relative IR Intensities of 1-, 2-, and 3-C$_{32}$H$_{15}^+$ Predicted with the B3PW91/6-311++G(2d,2p) Method[a]

Mode	Sym.	1-C$_{32}$H$_{15}^+$	2-C$_{32}$H$_{15}^+$	3-C$_{32}$H$_{15}^+$
ν_{15}	A'	1635 (32)[b]	1635 (17)[c]	1635 (8)[d]
ν_{16}	A'	1626 (37)	1623 (42)	1624 (31)
ν_{17}	A'	1620 (57)	1617 (75)	1621 (6)
ν_{18}	A'	1611 (3)	1609 (32)	1613 (15)
ν_{19}	A'	1608 (100)	1601 (10)	1604 (100)
ν_{20}	A'	1597 (41)	1597 (100)	1595 (19)
ν_{21}	A'	1579 (35)	1572 (5)	1581 (9)
ν_{22}	A'	1565 (22)	1554 (34)	1563 (13)
ν_{23}	A'	1536 (99)	1547 (21)	1542 (31)
ν_{24}	A'	1525 (19)	1534 (46)	1530 (14)
ν_{27}	A'	1488 (36)	1490 (8)	1492 (11)
ν_{36}	A'	1403 (38)	1407 (2)	1402 (5)
ν_{40}	A'	1377 (30)	1360 (42)	1370 (49)
ν_{41}	A'	1358 (98)	1352 (50)	1356 (27)
ν_{42}	A'	1355 (42)	1342 (10)	1355 (42)
ν_{43}	A'	1336 (54)	1329 (76)	1342 (32)
ν_{49}	A'	1238 (30)	1237 (18)	1243 (21)
ν_{50}	A'	1227 (32)	1228 (1)	1226 (2)
ν_{54}	A'	1193 (29)	1185 (1)	1189 (7)
ν_{64}	A'	1009 (20)	1008 (23)	1021 (15)
ν_{99}	A''	912 (27)	905 (30)	911 (22)
ν_{100}	A''	897 (19)	888 (18)	903 (5)
ν_{102}	A''	848 (26)	846 (26)	833 (14)

Notes.
[a] Scaling factors 0.958 and 0.978 were used for regions above and below 2500 cm^{-1}, respectively.
[b] Predicted IR intensities listed in parentheses are normalized to that of ν_{19} (201.9 km mol^{-1}).
[c] Predicted IR intensities listed in parentheses are normalized to that of ν_{20} (180.1 km mol^{-1}).
[d] Predicted IR intensities listed in parentheses are normalized to that of ν_{19} (300.9 km mol^{-1}).

(This table is available in its entirety in machine-readable form.)

The colors of the lines in the stick spectra in Figure 7 indicate the types of molecular vibrations associated with each band. These features near 6.2 μm are characteristic of the CC
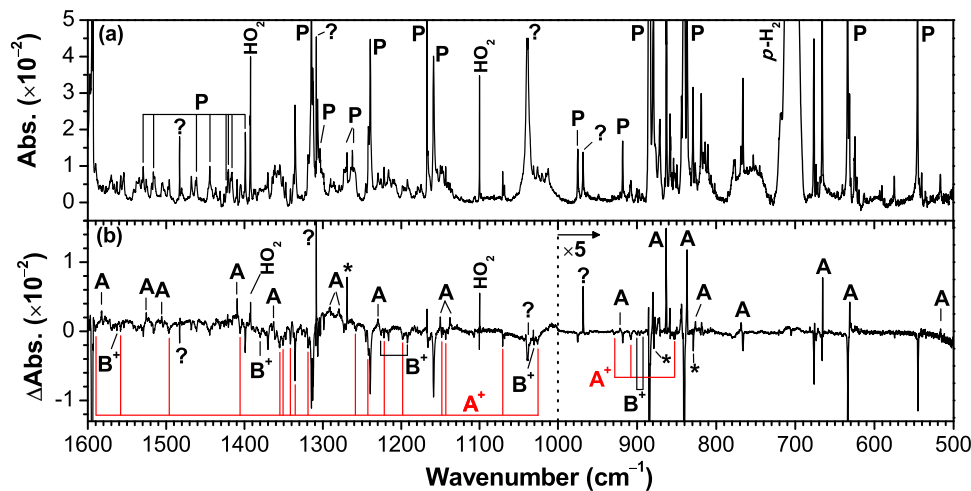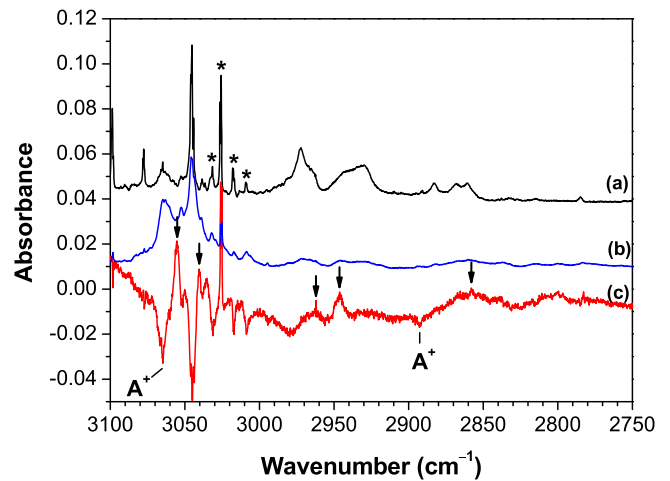

Figure 5. Partial IR spectra in the region 2750–3100 cm^{-1} of ovalene samples. (a) An ovalene/p-H$_2$ matrix deposited without electron bombardment, (b) an ovalene/p-H$_2$ matrix subjected to electron bombardment during deposition, and (c) a difference spectrum after maintaining the electron-bombarded ovalene/p-H$_2$ matrix in darkness for 20 hr. Lines belonging to group A (7-C$_{32}$H$_{15}$·) are indicated with arrows. Lines marked with * are from CH$_4$.

stretching mode of aromatic rings (blue). No significant shift is observed among 1-C$_{16}$H$_{11}^+$ (6.18–6.73 μm), 1-C$_{24}$H$_{13}^+$ (6.17–6.60 μm), and 7-C$_{32}$H$_{15}^+$ (6.20–6.68 μm), but particularly significant are the two intense combination bands (light blue) at 6.06 and 6.08 μm for 7-C$_{32}$H$_{15}^+$, slightly blueshifted from the peak of the UIR band at 6.2 μm. For the ring deformation mode (red), moderately intense lines are observed at 7.19, 7.37/7.27, and 7.49/7.11 μm for 1-C$_{16}$H$_{11}^+$, 1-C$_{24}$H$_{13}^+$, and 7-C$_{32}$H$_{15}^+$, respectively; the more intense lines are listed first. These lines follow the trend of redshift toward the peak of the UIR band at 7.7 μm. The CH$_2$ scissoring mode (green) is unique and characteristic of H$^+$PAH; this mode in 7-C$_{32}$H$_{15}^+$ was observed at 7.38 μm, near the corresponding lines at 7.45 μm for 1-C$_{16}$H$_{11}^+$ and 7.53 μm for 1-C$_{24}$H$_{13}^+$; these lines are within the region of the ring deformation modes.

The in-plane CH bending modes (black) of 1-C$_{16}$H$_{11}^+$ and 1-C$_{24}$H$_{13}^+$ are characterized by one intense line and a few

Figure 4. Partial mid-IR spectra of an electron-bombarded ovalene/p-H$_2$ matrix. (a) Spectrum recorded after deposition. (b) A difference spectrum after maintaining the matrix in darkness for 20 hr; lines pointing upward indicate production. The lines at 1100 and 1392 cm^{-1} originate from HO$_2$, the lines at 968, 1067, 1308, and 1483 cm^{-1} (indicated with ?) are due to unknown impurities from the sample, and the lines at 829, 879, and 1269 cm^{-1} (indicated with *) are unknown reaction products induced by electron bombardment. P: ovalene (C$_{32}$H$_{14}$); A: 7-C$_{32}$H$_{15}$·; A$^+$: 7-C$_{32}$H$_{15}^+$; B$^+$: unknown ionic species.
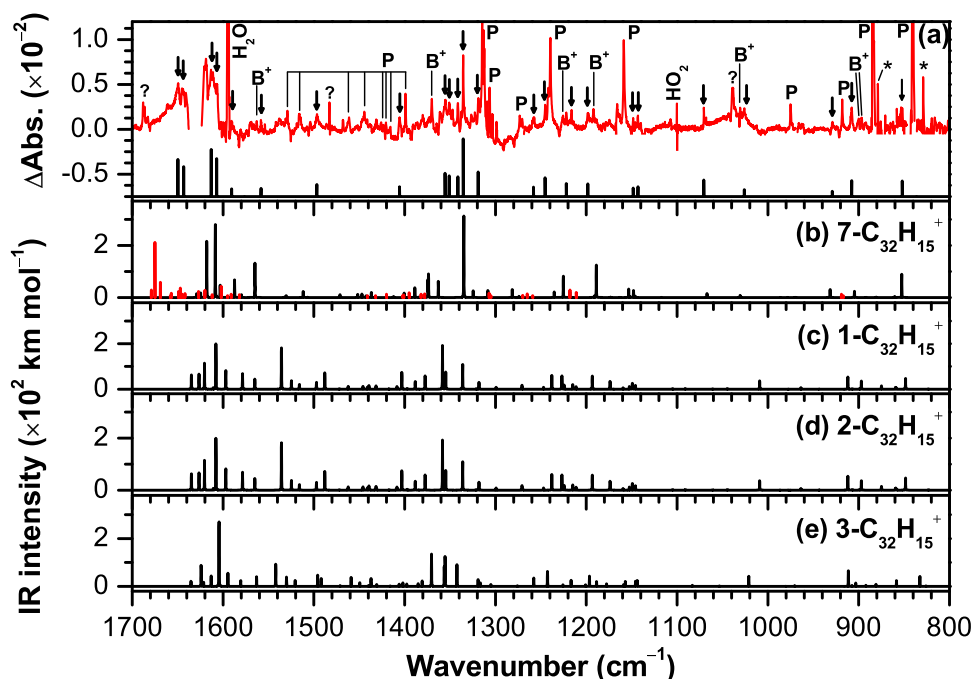
Figure 6. Comparison of lines in group A^+ with lines of various isomers of $C_{32}H_{15}$ predicted with theory. (a) A difference spectrum after maintaining the matrix in darkness for 20 hr; taken from Figure 4(b) and inverted. Lines in group A^+ are indicated with thin arrows and their stick spectrum is shown at the bottom of (a) for clarity. Lines due to unknown impurities and reaction products are marked with ? and *, respectively. An intense downward band near 1630 cm^{-1} is due to H_2O. Stick spectra of scaled ($\times 0.978$) harmonic vibrational wavenumbers predicted with the B3PW91/6-311++G(2d,2p) method are shown for (b) 7-$C_{32}H_{15}^+$, (c) 1-$C_{32}H_{15}^+$, (d) 2-$C_{32}H_{15}^+$, and (e) 3-$C_{32}H_{15}^+$. Combination bands of 7-$C_{32}H_{15}^+$ predicted with the anharmonic calculations using the B3PW91/6-31G(d,p) method are shown in red in (b).
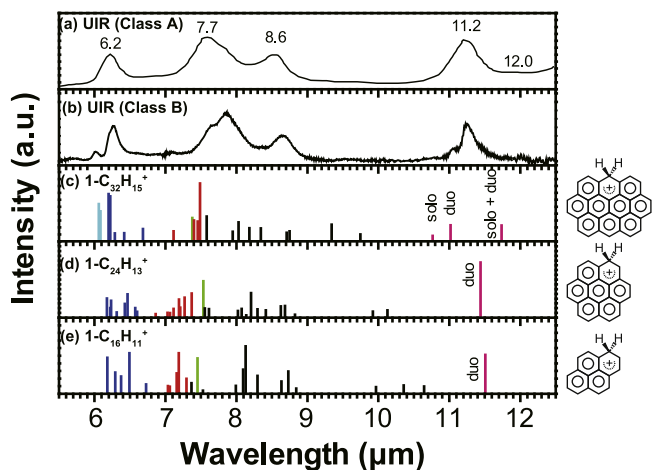

Figure 7. Comparison of UIR bands with observed spectra of H^+PAH. (a) UIR Class A spectrum observed from the Iris nebula, NGC 7023 (Cesarsky et al. 1996). (b) UIR Class B spectrum observed from the Red Rectangle, HD 44179 (Peeters et al. 2002). (c) Protonated ovalene (7-$C_{32}H_{15}^+$). (d) Protonated coronene (1-$C_{24}H_{13}^+$) (Bahou et al. 2014b). (e) Protonated pyrene (1-$C_{16}H_{11}^+$) (Bahou et al. 2013b). Experimental spectra are shown with sticks to represent relative peak intensities: pink, out-of-plane CH bend; black, in-plane CH bend; green, CH_2 scissor; red, ring deformation; blue, CC stretch; light blue, combination.

weaker ones, whereas those of 7-$C_{32}H_{15}^+$ are characterized by several lines with similar intensities that are spread across the 7.6–9.7 μm region. As a whole, the two lines of 7-$C_{32}H_{15}^+$ in the center (at 8.18 and 8.35 μm) seem to follow the trend of a redshift of the most intense lines from 1-$C_{16}H_{11}^+$ (8.13 μm) and 1-$C_{24}H_{13}^+$ (8.21 μm) toward the UIR bands at 8.6 μm.

Other features in the UIR bands are found at 11.2 (s), 12.0 (w), 12.6 (m), and 13.6 (w) μm, which are considered to originate from out-of-plane CH bending modes (pink) with active solo, duo, trio, and quartet hydrogens, respectively (Hony et al. 2001). The out-of-plane CH bending modes of 1-$C_{16}H_{11}^+$ and 1-$C_{24}H_{13}^+$ are observed at 11.51 and 11.44 μm, respectively; they are associated with motions of duo hydrogens. For 7-$C_{32}H_{15}^+$, as the line observed at 11.02 μm is assigned to be associated with duo hydrogens, the trend of blueshift for this mode as the size of the PAH increases is retained. A less intense line at 10.76 μm is also observed for 7-$C_{32}H_{15}^+$ and assigned to involve motion of the solo hydrogen. Both lines at 10.76 and 11.02 μm are slightly blueshifted from that of the intense UIR band at 11.2 μm, but fall within the envelope of the weak-to-moderate 11.0 μm band attributed to the out-of-plane CH bending modes of PAH cations (Hudgins & Allamandola 1999). The third feature of 7-$C_{32}H_{15}^+$ at 11.74 μm is assigned to the out-of-plane CH bending mode involving both solo and duo hydrogens, with coupling of a CH_2 rocking mode. This line is also slightly blueshifted from the weak UIR band at 12.0 μm. Lines corresponding to the UIR bands at 12.6 and 13.6 μm are unobserved in our experiments on 7-$C_{32}H_{15}^+$ because protonated ovalene has no trio and quartet hydrogens.

Considering the absorption bands of 1-$C_{16}H_{11}^+$, 1-$C_{24}H_{13}^+$, and 7-$C_{32}H_{15}^+$ in Figure 7, the spectral pattern of 7-$C_{32}H_{15}^+$ clearly matches best with the Class A UIR band envelopes in terms of positions and relative intensities. It is particularly interesting that these strongest lines in the protonated ovalene spectrum consistently fall on the blue side of the intense UIR feature profiles. Although these lines of 7-$C_{32}H_{15}^+$ are slightly blueshifted from those of the UIR bands with maxima near 6.2, 7.7, 8.6, 11.2, and 12.0 μm, the agreement is actually excellent

Table 4
Vibrational Wavenumber and Relative IR Intensities of Lines Observed for Protonated Pyrene (1-$C_{16}H_{11}^+$), Coronene (1-$C_{24}H_{13}^+$), and Ovalene (7-$C_{32}H_{15}^+$) in p-H_2 Matrices[a]

1-$C_{16}H_{11}^+$		1-$C_{24}H_{13}^+$		7-$C_{32}H_{15}^+$		UIR
(cm^{-1})	(μm)	(cm^{-1})	(μm)	(cm^{-1})	(μm)	(μm)
CC Stretch						
1618.0 (100)	6.18	1619.7 (32)	6.17	1649.7 (s)[b]	6.06[b]	6.2
1588.9 (18)	6.29	1607.4 (5)	6.22	1643.4 (s)[b]	6.08[b]	...
1568.7 (18)	6.37	1604.3 (17)	6.23	1613 (s)	6.20	...
1540.2 (41)	6.49	1584.4 (11)	6.31	1607 (s)	6.22	...
1486.5 (12)	6.73	1555.7 (22)	6.43	1590.5 (m)	6.29	...
		1546.8 (37)	6.46	1558.2 (m)	6.42	...
		1521.3 (19)	6.57	1496.7 (m)	6.68	...
		1514.8 (22)	6.60	...	...	...
Ring Deform						
1421.5 (10)	7.03	1457.2 (2) ?	6.86	1405.6 (17)	7.11	7.7
1416.4 (5) ?	7.06	1422.5 (7)	7.03	1351.0 (11)	7.40	...
1397.1 (14) ?	7.16	1415.7 (5)	7.06	1341.4 (12)	7.45	...
1391.3 (46)	7.19	1405.8 (10)	7.11	1335.5 (100)	7.49	...
1370.7 (13)	7.30	1390.5 (22)	7.19	...	...	...
...	...	1387.5 (10)	7.21	...	...	...
...	...	1375.7 (36)	7.27	...	...	...
...	...	1356.7 (100)	7.37	...	...	...
CH$_2$ Scissor						
1341.7 (31)	7.45	1327.2 (110)	7.53	1355.5 (13)	7.38	7.7
In-plane CH Bend						
1357.3 (5)	7.37	1323.7 (12)	7.55	1319.1 (26)	7.58	8.6
1328.3 (5)	7.53	1313.3 (10)	7.61	1258.1 (10) ?	7.95	...
1251.3 (10)	7.99	1246.7 (2) ?	8.02	1245.3 (9)	8.03	...
1235.6 (18)	8.09	1238.4 (3)	8.07	1221.9 (16)	8.18	...
1230.2 (38)	8.13	1228.9 (4)	8.14	1198.3 (11)	8.35	...
1205.1 (10)	8.30	1218.5 (55)	8.21	1148.3 (8) ?	8.71	...
1158.2 (6)	8.63	1205.3 (8)	8.30	1143.1 (10) ?	8.75	...
1145.3 (13)	8.73	1188.4 (6)	8.41	1070.6 (11)	9.34	...
1130.7 (3)	8.84	1159.4 (15)	8.63	1026.0 (11) ?	9.75	...
1003.2 (2) ?	9.97	1151.6 (12)	8.68	...	...	...
965.6 (2) ?	10.35	1133.0 (1)	8.83	...	...	...
939.3 (4)	10.64	1007.8 (22)	9.92	...	...	...
...	...	987.4 (6)	10.13	...	...	...
Out-of-plane CH Bend						
868.9 (29)	11.51	874.0 (111)	11.44	929.0 (25)	10.76	11.2
775.8 (2)	12.89	...	...	907.7 (32)	11.02	12.0
669.2 (3)	14.94	...	...	...	12.6	
...	...	...	...	...	...	13.6
Out-of-plane CH Bend + CH$_2$ Rock						
638.9 (7)	15.65	...	...	852.0 (26)	11.74	...
Ref. 1	...	Ref. 2	...	this work	...	Ref. 3

Notes.
[a] Relative integrated intensities are in parentheses; note that the stick spectra in Figure 7 represent relative peak intensities. Tentative assignments are indicated with "?."
[b] These lines are associated with combination transitions.
References. (1) Bahou et al. (2013b), (2) Bahou et al. (2014b), (3) Cesarsky et al. (1996).

when one considers the 10–30 cm^{-1} red-shifts associated with converting absorption to emission spectra.

The close resemblance of the spectral pattern of protonated ovalene with that of the UIR bands seems to indicate that H$^+$PAH can contribute to the prominent features of the UIR bands and might be important members of the interstellar PAH inventory. This is particularly significant because astronomical PAHs are considered to play important roles in the formation of

molecular hydrogen via H addition reactions (Bauschlicher 1998; Skov et al. 2014; Boschman et al. 2015). Spectral signatures characteristic of H$^+$PAH will enable observers to search for this component and probe their roles in the local environment. To reiterate, although pyrene and coronene are considered too small to survive the interstellar radiation field, ovalene lies at the lower end of the interstellar PAH size distribution and protonated ovalene may well be present

(Allamandola et al. 1989; Puget & Léger 1989). It would be desirable to extend this work to even larger PAHs to test if their spectra retain similar patterns.

REFERENCES

Allamandola, L. J., Tielens, A. G. G. M., & Barker, J. R. 1985, ApJL, 290, L25
Allamandola, L. J., Tielens, A. G. G. M., & Barker, J. R. 1989, ApJS, 71, 733
Bahou, M., Das, P., Lee, Y.-F., Wu, Y.-J., & Lee, Y.-P. 2014a, PCCP, 16, 2200
Bahou, M., Wu, Y.-J., & Lee, Y.-P. 2012, JChPh, 136, 154304
Bahou, M., Wu, Y.-J., & Lee, Y.-P. 2013a, PCCP, 15, 1907
Bahou, M., Wu, Y.-J., & Lee, Y.-P. 2013b, J. Phys. Chem. Lett., 4, 1989
Bahou, M., Wu, Y.-J., & Lee, Y.-P. 2014b, Angew. Chem. Int. Ed., 53, 1021
Basire, M., Parneix, P., Pino, T., Bréchignac, P., & Calvo, F. 2011, in PAHs and the Universe, ed. C. Joblin, & A. G. G. M. Tielens (Les Ulis: EAD Sciences), 95
Bauschlicher, C. W., Jr 1998, ApJL, 509, L125
Bauschlicher, C. W., Jr, & Bakes, E. L. O. 2000, CP, 262, 285
Becke, A. D. 1993, JChPh, 98, 5648
Bloino, J., & Barone, V. 2012, JChPh, 136, 124108
Boersma, C., Bregman, J. D., & Allamandola, L. J. 2013, ApJ, 769, 117
Boschman, L., Cazaux, S., Spaans, M., Hoekstra, R., & Schlathölter, T. 2015, A&A, 579, A72
Bouwman, J., Cuppen, H. M., Bakker, A., Allamandola, L. J., & Linnartz, H. 2010, A&A, 511, A33
Brenner, J. D., & Barker, J. R. 1992, ApJL, 388, L39
Cesarsky, D., Jequeux, J., Abergel, A., et al. 1996, A&A, 315, L305
Cook, D. J., & Saykally, R. J. 1998, ApJ, 493, 793
Cook, D. J., Schlemmer, S., Balucani, N., et al. 1996, Natur, 380, 227
Dopfer, O. 2011, in PAHs and the Universe, ed. C. Joblin, & A. G. G. M. Tielens (Les Ulis: EAD Sciences), 103
Douberly, G. E., Ricks, A. M., Schleyer, P. V. R., & Duncan, M. A. 2008, JPCA, 112, 4869

Ehrenfreund, P., d"Hendecourt, L., Verstraete, L., et al. 1992, A&A, 259, 257
Frisch, M. J., Trucks, G. W., Schlegel, H. B., et al. 2009, Gaussian 09 (Wallingford, CT: Gaussian, Inc.) Revision D.01 http://www.Gaussian.com
Hammonds, M., Pathak, A., & Sarre, P. J. 2009, PCCP, 11, 4458
Hony, S., Van Kerchhoven, C., Peeters, E., et al. 2001, A&A, 370, 1030
Hudgins, D. M., & Allamandola, L. J. 1999, ApJL, 516, L41
Hudgins, D. M., Bauschlicher, C. W., Jr, & Allamandola, L. J. 2001, AcSpA, 57, 907
Joblin, C., Boissel, P., Léger, A., d'Hendecourt, L., & Défourneau, D. 1995, A&A, 299, 835
Joblin, C., d'Hendecourt, L., Léger, A., & Défourneau, D. 1994, A&A, 281, 923
Jones, W., Boissel, P., Chiavarino, B., et al. 2003, Angew. Chem. Int. Ed., 42, 2057
Knorke, H., Langer, J., Oomens, J., & Dopfer, O. 2009, ApJL, 706, L66
Langhoff, S. R. 1996, JPhCh, 100, 2819
Lee, Y.-P., Wu, Y.-J., Lees, R. M., Xu, L.-H., & Hougen, J. T. 2006, Sci, 311, 365
Leger, A., & Puget, J. L. 1984, A&A, 137, L5
Malloci, G., Mulas, G., Cappellini, G., Fiorentini, V., & Porceddu, I. 2005, A&A, 432, 585
Malloci, G., Mulas, G., & Joblin, C. 2004, A&A, 426, 105
Mattioda, A. L., Ricca, A., Tucker, J., Bauschlicher, C. W., Jr., & Allamandola, L. J. 2009, AJ, 137, 4054
Pathak, A., & Sarre, P. J. 2008, MNRAS, 391, L10
Pech, C., Joblin, C., & Boissel, P. 2002, A&A, 388, 639
Peeters, E., Hony, S., Kerckhoven, C. V., et al. 2002, A&A, 390, 1089
Perdew, J. P., Burke, K., & Wang, Y. 1996, PhRvB, 54, 16533
Puget, J. L., & Léger, A. 1989, ARA&A, 27, 161
Ricca, A., Bauschlicher, C. W., & Allamandola, L. J. 2011, ApJ, 727, 128
Ricks, A. M., Douberly, G. E., & Duncan, M. A. 2009, ApJ, 702, 301
Ruiterkamp, R., Halasinski, T., Salama, F., et al. 2002, A&A, 390, 1153
Skov, A. L., Thrower, J. D., & Hornekaer, L. 2014, FaDi, 168, 223
Snow, T. P., Le Page, V., Keheyan, Y., & Bierbaum, V. M. 1998, Natur, 391, 259
Solcà, N., & Dopfer, O. 2002, Angew. Chem. Int. Ed., 41, 3628
Steglich, M., Bouwman, J., Huisken, F., & Th, H. 2011, ApJ, 742, 2
Tielens, A. G. G. M. 2011, in PAHs and the Universe, ed. C. Joblin, & A. G. G. M. Tielens (Les Ulis: EAD Sciences), 3
Weisman, J. L., Lee, T. J., Salama, F., & Head-Gordon, M. 2003, ApJ, 587, 256
Williams, R. M., & Leone, S. R. 1995, ApJ, 443, 675
Willner, S. P. 1984, in Galactic and Extragalactic Infrared Spectroscopy, ed. M. F. Kessler, & J. P. Phillips (Dordrecht: Reidel), 37